ARTICLE

Synthesis and Sensing Efficiency of Bioinspired CN Wrapped $ZnFe_2O_4$ Microspheres-Ionic Liquid Composite Towards Ultra-High Sensitivity Arsenic(III) Monitoring of Ground Drinking Water

Received 00th January 20xx,
Accepted 00th January 20xx

DOI: 10.1039/x0xx00000x

Awais Siddique Saleemi,[ab] Muhammad Hafeez,[b] Aqsa Munawar,[c] Naeem Akhtar,[d] Waseem Abbas,[e] Muhammad Ehsan Mazhar,[e] Zahid Shafiq,[c] Anthony P. Davis,[f] Shern-Long Lee,[a*]

Arsenic(III) poisoning may lead to neurological disorders, heart diseases or carcinogenic effects due to long-term exposure. The presence of arsenic in drinking water is a widespread problem and presents an important analytical challenge. Among the methods for As(III) monitoring, electrochemical analysis offers fast response, low detection limits and high sensitivity. Here we report a novel system which achieves exceptional performance without use of expensive noble metals by exploiting a metal oxide rich in oxygen vacancies (OVs). Novel OVs rich spinel $ZnFe_2O_4$ micro-spheres (ZF-Ms) were synthesized and applied to electrochemical monitoring of As(III) in underground drinking water by using square wave anodic stripping voltammetry (SWASV) in acetate buffer (pH 6.0). To boost sensing capability, the surface of ZF-Ms were further wrapped with bioinspired carbon and nitrogen rich nano-dots (CN) and modified with benzimidazolium-1-acetate ionic liquid (IL). The designed bioinspired CN wrapped IL modified ZF-Ms (CN@ZF-Ms-IL) sensor offered an ultra-low detection limit of 0.0006 ppb (based on the 3σ method), high sensitivity (41.08 μA ppb^{-1}) and a wide linear range (~1-60 ppb) including the World Health Organization (WHO) desirable range (10 ppb). To the best of our knowledge, the system outperforms most alternatives based on noble metal electrodes and almost all metal-free based reported electrochemical sensors. A possible sensing mechanism is proposed and supported with experimental evidence. Additionally, the system has been successfully applied to monitor arsenic-contaminated real ground drinking water collected from a flood affected area, Muzaffargarh, Punjab, Pakistan.

Introduction

Clean water, free of contaminants, is a prerequisite for human health.[1] Among potential contaminants arsenic (As) presents an important challenge for analytical chemists, because of its widespread occurrence and high toxicity even at very low concentrations levels. Prolonged exposure to As may result in serious health problems such as neurological disorders, heart diseases, carcinogenic effects (bladder, lung, prostate, kidney, skin, liver and nasal cancer), diabetes mellitus, hypertension, bronchitis, chronic airway obstruction, and growth defects.[2] According to the reported literature, nearly 20 countries have arsenic contaminated drinking water with As levels greater than World Health Organization (WHO) and the U.S. Environmental Protection Agency guideline value of 10 μg L^{-1}.[3] Arsenic exists in the environment in various oxidation states (−3, 0, +3, and +5), but in natural waters it is mostly found in inorganic form as trivalent arsenite [As(III)] or pentavalent arsenate [As(V)].[4] Of these, As(III) is reported to be the most toxic [25-60 fold compared to As(V)].[5] Thus, the development of an accurate, fast, highly sensitive and selective sensor to detect As(III) in drinking water is a high priority.

A wide range of accurate monitoring techniques such as oxidation, ion-exchange, atomic absorption spectroscopy, inductively coupled plasma mass spectrometry (ICPMS) and hydride generation atomic fluorescence spectrometry have been successfully implemented to monitor arsenic in drinking water.[6] However, most of these techniques employ expensive and complicated instruments, require well-trained engineers to perform the measurements, are time-consuming and suffer from poor stability. They are therefore mainly unsuitable for on-site monitoring of multiple samples. By contrast, the electrochemical methods which have been developed over the past decade are more promising, offering on-site capability, ease of use and low cost.[2, 3, 7] According to the reported literature, hanging mercury drop and mercury film electrodes have been successfully applied for the highly sensitive electrochemical monitoring of As(III).[8] However, later these were replaced with solid metals including gold (Au), platinum

[a.] *Institute for Advanced Study, Shenzhen University, Shenzhen 518060, Guangdong, China. E-mail: sllee@szu.edu.cn*
[b.] *Key Laboratory of Optoelectronic Devices and Systems of Ministry of Education and Guangdong Provence, College of Optoelectronic Engineering, Shenzhen University, Shenzhen 518060, Guangdong, China.*
[c.] *Institute of Chemical Sciences, Bahauddin Zakariya University (BZU) Multan 60800, Pakistan*
[d.] *Interdisciplinary Research Centre in Biomedical Materials (IRCBM), COMSATS University Islamabad, Lahore Campus, Lahore 54000, Pakistan*
[e.] *Department of Physics, Bahauddin Zakariya University, Multan, 60800, Pakistan*
[f.] *School of Chemistry, University of Bristol, Cantock's Close, Bristol BS8 1TS, UK*
† Footnotes relating to the title and/or authors should appear here.
Electronic Supplementary Information (ESI) available: [details of any supplementary information available should be included here]. See DOI: 10.1039/x0xx00000x

(Pt) and silver (Ag) to overcome the potential toxicity and operational limitations of mercury.[9] Gold based electrodes gained more interest compared to platinum (Pt) and silver (Ag), because of enhanced catalytic performance towards As. Although these sensors have promising features, commercialization has been hampered by factors including (i) high cost, (ii) strongly acidic (e.g. HCl, H_2SO_4, $HClO_4$ and HNO_3) operational condition that could produce toxic arsine gases, (iii) complexity in fabrication and (iv) surface fouling.

To overcome these limitations, several noble metal-free electrodes have been used successfully to monitor As(III), in some cases using non-acidic electrolytes. For example, Cox and Kulesza fabricated thin films of mixed-valent ruthenium(III, II) cyanide at glassy carbon electrodes for precise monitoring of As(III), using 0.5 M NaCl (pH = 2) as an electrolyte.[10] Similarly, boron doped iridium oxide coated diamond electrodes have been successfully applied for amperometric detection of As(III) in phosphate buffer (pH = 4.30) by Salimi et al.[11] Recently, low-cost, environmentally friendly, monodispersed Fe_3O_4 microspheres with strong adsorption capability were exploited to monitor the As(III) from drinking water with high efficacy.[3] To increase conduction pathways for electrons on the electrode surface, the Fe_3O_4 microspheres were modified with ionic liquids, leading to better electrochemical performance than commonly used noble metals.

Recently, the use of spinel zinc ferrite ($ZnFe_2O_4$) has attracted great interest as a functional n-type semiconductor that could be efficiently used in water-splitting and photocatalytic degradation of pollutants, by acting respectively as a photoelectric material or a surface catalyst.[12] $ZnFe_2O_4$ is rich in oxygen vacancies (OVs), leading to high conductivity, and we reasoned that an electrochemical As(III) sensor based on this material could perform exceptionally well.[13] The high conductivity should (i) help to prevent charge resistance (created as a result of adsorption of target molecules at the surface) between conduction and valence band, (ii) minimize the problem of surface fouling and (iii) lead to high sensitivity. Here we report the use of OV-rich $ZnFe_2O_4$ microsphere (ZF-Ms) modified graphitic electrodes (GE) for precise monitoring of As(III) in acetate buffer (pH 6.0). The presence of OVs leads to increased charge transfer and provides more active sites for adsorption of As(III) species, thus resulting in enhanced electrical conductivity and improving the oxidation-reduction reaction. To optimize performance the ZF-Ms were further wrapped with bioinspired carbon and nitrogen rich nano-dots (CN), prepared via a novel process, and modified with benzimidazolium-1-acetate ionic liquid (IL). The bioinspired CN wrapping incorporates edge plane defects, whereas the IL provides high pi electron density to the ZF-Ms based sensing system, thus resulting in reduced electronic transition resistance and fast shuttling of electrons through smooth conduction pathways. This new noble metal-free system offers excellent sensing (41.08 μA ppb^{-1}) and good selectivity towards As(III) in non- acidic solution (acetate buffer :pH 6.0), better than most noble metal-based and almost all reported metal-free electrochemical sensors as far as we know. A possible adsorption mechanism is also proposed with support from experimental and theoretical evidences. Our results further reveal that the sensor could successfully be applied to the selective and sensitive monitoring of As(III) from arsenic contaminated real ground water samples collected from a flood-affected area, Muzaffargarh, Punjab, Pakistan. To the best of our knowledge, this is the first application of CN@ZF-Ms-IL modified GP electrodes in a system for electrochemical As(III) monitoring .

2 Results and discussion

2.1 Morphological and compositional characterization of ZF-Ms

Apart from composition, the shape and morphology of a material also play a vital role in controlling the electrochemical properties, by modifying the electron transport route and exposing more catalytic sites.[14] Thus, the morphological feature of the synthesized material was characterized through scanning electron microscopy (SEM), transmission electron microscopy (TEM) and high-resolution transmission electron microscopy (HR-TEM). SEM images (Figure 1A) indicate uniform formation of $ZnFe_2O_4$ with budded spherical shape morphology at micro scale level. The size of the $ZnFe_2O_4$ budded microspheres (ZF-Ms) were observed to be in the range of ~350-400 nm. A high magnification image (Figure 1B) further shows a cracked and rough microsphere surface with textured buds. A TEM image (Figure 1C) reveals that the surface of the microsphere is composed of nanosphere (~10-20 nm) building blocks which are internally inter-connected with the core of sphere. Figure 1E shows the HR-TEM analysis of the ZF-Ms with clear crystal facets. The corresponding inverse fast Fourier transform (IFFT) image (Figure 1F) indicates lattice fringes with d spacing of 0.24, matching well with the lattice spacing of the atomic planes of the cubic, Fd-3m (227). Coating of the ZF-MS with bioinspired CN nanodots (~10-15 nm) is clearly visible from SEM (Figure 1G and Figure S4A) and TEM (Figure 1D) images. Similarly, modification of CN@ZF-Ms with IL is also clearly visible from Figure S4B.

Figure 1

The phase purity and crystallographic structure of the ZF-MS and CN@ZF-Ms were investigated by means of XRD (Figure S5A). All the diffraction peaks at (111), (220), (311), (222), (400), (422), (511) and (533) correspond to the face-centered cubic structure of ZF-MS with Fd3m space group (Figure S5A-a). These results match well with the lattice planes of cubic structured spinel $ZnFe_2O_4$ (JCPDS card no. 022-1012). Similarly, the XRD profile of CN@ZF-Ms also matches well with cubic structured spinel $ZnFe_2O_4$, with the exception of an additional carbon broad peak at $2\Theta = 24.68$ (Figure S5A-b).[15]

Raman measurements were further used to investigate the structure and phase phenomena of the synthesized ZF-Ms and CN@ZF-Ms (Figure S5-B). Results indicate that both ZF-Ms and CN@ZF-Ms, with Fd3m space group, show five Raman active modes (A_{1g} ⍰ E_g ⍰ $3F_{2g}$), matching well with the reported literature.[16] The modes above 600 cm^{-1} mostly correspond to the movement of oxygen at tetrahedral site (AO_4) in cubic spinal ferrite. Thus, the mode at 609 cm^{-1} is attributed to A_{1g} symmetry. The Raman active modes at low frequency are

related to the octahedral sites (BO_6).[17] The appearance of two distinct bands ~1370 and 1585 cm^{-1} correspond to the existence of disordered carbon (D) and quasi-graphitic carbon (G) at the surface of CN@ZF-Ms. To estimate carbon hybridization, intensity ratio IG/ID was calculated and was observed to be 0.90. These results suggest firm attachment of CN at the surface of ZF-Ms with plentiful defects and are in good agreement with the reported literature.[18]

Scheme 1

X-ray photoelectron spectroscopy (XPS) analysis was further performed to gain additional insight into CN@ZF-Ms (Figure 2). The wide range survey spectra contain peaks corresponding to all components of CN@ZF-Ms including Zn, Fe, O, C and N (Figure 2A). High resolution XPS spectra indicate two distinct peaks of Zn 2p, located around ~1044.5 and 1021.7 eV corresponding to $Zn2p_{1/2}$ and $Zn2p_{3/2}$ bands, respectively (Figure 2B). High resolution XPS spectrum of Fe2p (Figure 2C) shows three distinct peaks corresponding to $Fe2p_{1/2}$ (~724.5 eV), $Fe2p_{3/2}$ (~712.6 eV) and $Fe2p_{3/2}$ (~710.5 eV). The two peaks of $Fe2p_{3/2}$ suggest the existence of both octahedral and tetrahedral sites.[19] Tetrahedral coordination is expected at Zn-O sites, where Fe ions replace the Zn ions, whereas Fe-O sites are octahedral. A satellite peak (~719.1 eV) is also observed in the middle of the Fe $2p_{1/2}$ and Fe $2p_{3/2}$ peaks.[20] Figure 2D shows high resolution XPS spectra of O1s. O1s shows three distinct fitting peaks located around 530.2, 531. 5 and 532. 7 eV corresponding to lattice oxygen (OL), oxygen vacancy (Ov) and surface adsorbed oxygen (OC) respectively. According to the reported literature, the presence of the Ov peak not only leads to an increase in adsorption capability by providing more active adsorption sites, but also donates more free electrons to maintain high carrier mobility, thus resulting in enhanced sensing performance.[26] High resolution XPS spectra of C 1s (Figure 2E) shows four strong fitting peaks of C-C (sp^2), C-C (sp^3), C=O and O-C=O bands, at around 284.8, 285.4, 288.6 and 288.8 eV, respectively. Similarly, N 1s spectra show four main peaks centered at 398.6, 399.4, 400.3 and 402.4 eV assigned to pyridinic nitrogen (C=N), pyrrolic nitrogen (C-N), graphitic nitrogen and N-oxide of pyridinic nitrogen, respectively (Figure 2F). The existence of pyridinic nitrogen may result from defects, which have a direct impact on ion mobility at the electrode-electrolyte interface.

2.2 Electrocatalytic assessments of ZF-Ms, CN@ZF-Ms and CN@ZF-Ms-IL

To investigate the influence of structural variations on the electrochemical catalytic capability of the new materials ZF-MS, CN@ZF-MS and CN@ZF-MS-IL, as well as bare graphite, were examined through cyclic voltammetry in 0.1M KCl solution, using 5 mM of $[Fe(CN)_6]^{3-/4-}$ as a redox probe (Figure S6-A). A pair of redox peaks appear at all four different electrodes at an applied scan rate of 50 mVs^{-1} in the potential range from -0.4 to 0.4 V. Results (Figure S6-A) indicate that the bare graphitic electrode (GE) displays a small redox peak current intensity which is significantly enhanced by modifying the surface with electrically conductive OVs rich ZF-Ms, as evidenced from Figure 2D. The peak intensity increases linearly further in terms of current density at the surface of CN@ZF-Ms and CN@ZF-Ms-IL. Additionally, it is also evident that CN@ZF-Ms-IL (0.09) has a lower peak to peak potential difference compared to bare GE (0.14 V), ZF-Ms (0.11) and CN@ZF-Ms (0.10). This variation in interfacial properties of ZF-MS, CN@ZF-MS and CN@ZF-MS-IL modified electrodes were further investigated through impedance spectroscopy in 0.1 M aqueous KCl solution containing 5 mM of [Fe (CN)6]3-/4-. Nyquist plots of ZF-Ms, CN@ZF-Ms and CN@ZF-Ms-IL modified electrodes are shown in Figure S6-B. The results indicate two distinct regions, semicircular and linear. The semicircular part in the high frequency region corresponds to an electron transfer resistive process, whereas the linear portion in the low frequency region is associated with the diffusion process. The spectrum further reveals that CN@ZF-Ms-IL has lowest semicircular portion (206 Ω) compared to CN@ZF-Ms (382 Ω) and ZF-Ms (646 Ω). The high electrocatalytic efficiency of the CN@ZF-Ms-IL could be attributed to, (i) the incorporation of edge plane defects after CN coating, which reduce the electronic transition resistance and facilitate the movement of electrons, (ii) high pi electron density provided by the IL, because of presence of aromatic rings (benzimidazole cation) and carboxylate functional groups. The impact of the CN and IL on the electrochemically active electrode surface of ZF-Ms was further confirmed through the Randles-Sevcik equation,[21]

$$ip = 2.69 \times 10^5 A\, n^{3/2}\, D_o{}^{1/2}\, C^*\, v^{1/2}$$

Where, C^* is the concentration of ferrocyanide (5×10^{-3} mol/cm^3), D_o is the diffusion coefficient of potassium ferrocyanide (7.6×10^{-6} cm^2s^{-1}) and v is the scan rate. The electrochemically active surface areas of the ZF-Ms, CN@ZF-Ms and CN@ZF-Ms-IL are calculated to be 0.0815, 0.0962 and 0.174 cm^{-2} respectively (Figure S7).

2.3 Sensing efficiency of the designed ZF-Ms, CN@ZF-Ms and CN@ZF-Ms-IL towards As(III)

Square-wave anodic stripping voltammetry (SWASV) was applied under optimized experimental conditions (Figures S8, S9 & S10): frequency, 30 Hz; amplitude, deposition time (120 s) and deposition potential -0.45V, to assess the electrocatalytic performance of ZF-Ms, CN@ZF-Ms and CN@ZF-Ms-IL towards As(III) in 0.1 M acetate buffer (pH = 6). The corresponding SWASV responses are shown in Figure 3. The results indicate that increasing the concentration of As(III) in the electrolyte leads to increases in stripping peak current responses for all three electrodes (Figure 3A, 3C & 3E). The stripping peak current can be ascribed to the electrooxidation of As(III). Calibration plots of analyte concentration versus stripping peak current response for all three electrodes were derived from their respective SWASV results (Figures 3B, 3D & 3F). The regression equation for ZF-Ms obtained by fitting is given as i(μA) = 20.16x (ppb) +27.169 with correlation coefficient R^2 = 0.997. The remarkably high sensitivity (20.16 μA ppb^{-1}) of this electrode implies a theoretical limit of detection (LOD) value of 0.0012 ppb (based on the 3σ method), which compares well with reported sensors (Table S1). The

enhanced sensing efficiency could be attributed to the high absorption ability of the ZF-Ms toward As(III) because of the availability of more oxygen vacancies (O_{VS}), as evidenced from Figure 2D, that not only provide more adsorption active sites but also donate more free electrons to maintain high carrier mobility. Interestingly, the sensitivity of the ZF-Ms is increased by ~1.4 fold (29.17 μA ppb^{-1}) upon coating with CN nano-dots, which incorporate edge plane defects and facilitate the movement of ions. Additionally, higher value of correlation coefficient (R^2 = 0.998) with better LOD of 0.00092 ppb (based on 3σ method) is obtained from fitting of the linearization equation [*i*(μA) = 29.17x (ppb) +27.031, R^2 = 0.998]. Finally, modification of CN@ ZF-Ms with IL leads to a further increase in conduction pathways, resulting in even greater sensitivity. The fitted linearization equation [*i*(μA) = 41.08x (ppb) +45.31, R^2 = 0.999] shows that the sensitivity is increased by ~2.03-fold (41.08 μA ppb^{-1}) relative to ZF-Ms, with a higher correlation coefficient R^2 = 0.999 and a remarkable LOD of 0.0006 ppb (based on the 3σ method). The observed LOD is much better than most of the reported noble metal and almost all non-noble metal-based electrochemical sensors as far as we know (Table S1). To obtain the linear range, the concentration of As(III) was further increased up to 80 ppb for CN@ZF-Ms-IL (Figure S11) and the results indicate a wide linear range up to 60 ppb. It is worth mentioning that with increasing As(III) concentration, the peak current is shifted to a more positive potential at all three electrodes. This could be attributed to, (i) overlapping of diffusion layers produced as a result of stripping of the As(0) to As(III) in solution, according to Compton's group, and also (ii) increasing the concentration of As(III) in a system with more electrodeposited As(0) leads to a decrease in the activity coefficient, thus requiring a longer sweep as predicted by Debye–Hückel theory.[3]

Figure 2
Scheme 2

2.4 As(III) Sensing mechanism of our designed system

The method of synthesis used for ZF-Ms, and the appearance of Fe2p peaks in Figure 2C, suggest the formation of a mixed or inverse spinal ferrite as supported by Mossbauer theory. Thus, Fe-ions (Fe^{2+} and Fe^{3+}) are located on both octahedral and tetrahedral sites. The tetrahedral sites are enriched with Fe^{3+} ions whereas the octahedral sites accommodate both Fe^{2+} and Fe^{3+} ions.[22] During electrochemical sensing, the OVs-rich ZF-Ms offers numerous active octahedral sites for the adsorption of As (III) 3d ions, resulting in the reduction of As(III) to As(0). The stripping peak current results from oxidation of As(0) into As (III) (Scheme 2).[23] The incorporation of CN, and further modification with IL leads to rapid shuttling of electrons by acting as an electron transport mediator, and prevents long term accumulation of metal ions on the surface, resulting in highly efficient system. The efficiency of the Zn-MS, CN@ZF-Ms and CN@ZF-Ms-IL electrodes can be evaluated by how well these can adsorb As(III), as this has a direct impact on the stripping peak current. We have therefore performed XPS analysis on the materials after exposure to As(III), to determine their adsorption efficiency (Figure S12). The samples were prepared by dipping Zn-MS, CN@ZF-Ms and CN@ZF-Ms-IL electrodes for 5 min into 0.1 M acetate buffer containing a high concentration (500 ppb) of As(III). A high concentration of As(III) was selected to obtain better XPS resolution. The high resolution XPS spectra indicate that a clear peak of As 3d appears with varying intensity at all three electrodes. These results suggest that incorporation of CN and further modification with IL have positive impacts on the adsorption of As(III), as well as increasing conduction pathways, thus resulting in high sensitivity.

Figure 3

2.5 Selective efficiency of the designed CN@ZF-Ms-IL towards As(III) monitoring

The electrochemical selective monitoring of As(III) ions in real water samples is a challenging task because interfering species are coprecipitated and stripped off under the applied experimental conditions. Interfering species present in real water samples include Cu(II), Pb(II) and Hg(II). Among these metal ions Cu (II) is the major interfering agent because of the formation of intermetallic Cu_3As_2 species that generate competition for adsorption against As(III).[24] Thus, we analyzed the impact of Cu(II) on the electrochemical sensing efficiency of the CN@ZF-Ms-IL electrode using SWASV under optimized conditions. Figure 4A shows the stripping peak current response of CN@ZF-Ms-IL towards 10 ppb of As(III) in the presence of increasing concentration (20-60 ppb) of Cu(II). The results indicate that the stripping peak current response decreases insignificantly even upon adding high concentration of Cu(II). The corresponding % loss of the arsenic stripping peak current versus concentration of Cu(II) is shown in Figure 4B. The current decreases by just ~20% for 10 ppb of As (II) even after addition of 60 ppb of Cu(II). Additionally, a clear stripping peak potential difference is also obvious.

Similarly, we used SWASV to measure the impact of Hg(II) and Cd(II) on the selective efficiency of CN@ZF-Ms-IL towards As(III). Figure 4C shows the stripping peak current response of CN@ZF-Ms-IL towards increasing concentrations of Hg(II), Cd(II) and As(III) in 0.1 M acetate buffer (pH = 6). A significant peak potential difference is observed between the three analytes even upon increasing the concentration of all analytes simultaneously, thus these analytes could also be detected. The sensitivity to all three analytes was calculated from a plot of peak current versus concentration (Figure 4D). The sensitivity obtained for As(III) is approximately 95 and 103 times higher than for Cd(II) and Hg(II) respectively, supporting the reliability of our system.

Figure 4

2.6 Real time monitoring of As(III) from ground drinking water

To evaluate the practical applicability of the CN@ZF-Ms-IL electrode, As(III) contaminated real drinking water samples were collected from a flood affected area in Pakistan (Figure 5A). The samples were collected in precleaned polyethylene bottles (1.5 L capacity) from hand pumps or motorized pumps following standard procedures and were analysed by the Soil and Water Testing Lab of M. Garh, Pakistan (Table S2) using the MERCK 117917 Arsenic Test kit. Samples with arsenic levels 2.5 (25 ppb) and 5 times (50 ppb) higher value than WHO (10 ppb) guideline were selected to evaluate the efficiency of the designed CN@ZF-Ms-IL sensor. The samples were labelled as P1

(25 ppb) and P2 (50 ppb). These real samples were diluted with 0.1 M acetate buffer (pH 6.0) in a ratio of 1:99. No further sample treatment was performed. The stripping current responses of our CN@ZF-Ms-IL sensor are shown in Figure 5B. The results obtained using our designed systems were 27 and 56 ppb, for P1 and P2 samples respectively. In comparison, analysis by ICPMS gave values of about 32 and 59 ppb (Figure 5D). The slightly higher values from ICPMS could be due to the presence of As(V), which was not detected by our system. In any case the discrepancies are small, and these results support the reliability of our designed CN@ZF-Ms-IL system.

Figure 5

3. Conclusions

In the present study, we successfully synthesized novel OVs-rich spinel ZF-Ms by a simple solvothermal approach, and used them to achieve highly efficient electrochemical sensing of As(III) in drinking water. To optimize performance, the surface of the ZF-Ms was wrapped with CN dots (to incorporate edge plane defects) and modified with IL (to provide high pi electron density). Electrodes modified with this material gave selective and direct monitoring of As(III) within the WHO recommended range (around 10 ppb). Apart from its simplicity and low cost, the method provides reliable selectivity and excellent sensitivity over wide linear range. The sensitivity and limit of detection are better than most noble metal based and almost all metal-free based reported electrochemical sensors, as far as we know. The CN@ZF-Ms-IL electrodes have been successfully employed for the precise monitoring of arsenic in ground drinking water and, with further development, would seem to have potential for real-world application.

4. Experimental

4.1 Materials and chemicals

Zinc chloride, calcium chloride, iron chloride, ethylene glycol, and sodium acetate were purchased from Shanghai Macklin Biochemical Co., Ltd. China. Benzimidazole AR was purchased from Aladdin Industrial Corporation, (Shanghai, China). Sodium (meta) arsenite (90%) and cupric sulfate were purchased from Sigma-Aldrich. All reagents were of analytical grade and used as received. Deionized water was used to prepare all the solutions.

4.2 Synthesis of ZF-Ms

The spherical shaped ZF-Ms were synthesized through a solvothermal approach. Briefly, stoichiometric amounts of $ZnCl_2$ (2 mM), $FeCl_3$ (4 mM) and sodium acetate (0.04 M) were dissolved in 60 ml of ethylene glycol and vigorously stirred overnight. Subsequently, the solution was transferred into 100 ml PPL lined autoclaves for solvothermal reaction at 220 °C for 18 h. After cooling to room temperature, the autoclaves were opened, and products were separated from the reaction mixture by centrifugation. The products were washed with ethanol and distilled water several time with the help of sonication and centrifugation. The samples were dried in an oven at 80 ^oC for 24 h, then ground to fine powder with a mortar and pestle.

4.3 Synthesis of bioinspired CN@ZF-Ms

To prepare the bioinspired CN we selected, for the first-time, a mixture of xanthine and dopamine (ratio 1:1) as a source of C and N (Scheme 1). Dopamine was selected because of its easy polymerization in air, which helps in maintaining the shape of the synthesized material, whereas xanthine is rich in N (36.8 %, compared to dopamine at 9.1 %). Thus, a solution of dopamine (4 mg) and xanthine (4 mg) was prepared in phosphate buffer (100 mL) in a 250 mL volumetric flask, with stirring at room temperature for 2 minutes. 10 mg of synthesized ZF-Ms material was then added to the stirred solution to facilitate polymerization. Polymerization was performed for 6 h at room temperature, and the obtained dopamine-xanthine polymerized ZF-Ms material was washed several times with deionized water. The product was calcined at 500 °C for 4 h in an argon atmosphere to obtain CN@ZF-Ms.

4.4 Synthesis of Benzimidazolium-1-acatate ionic liquid (IL)

Benzimidazolium-1-acatate ionic liquid (IL) was synthesized by the neutralization of benzimidazole with the acetic acid. Briefly, 16.9 mmol of benzimidazole was added to 10 mL of methanol in two neck boiling flask and the mixture was vigorously stirred at 64 °C. Next, 0.965 mL of acetic acid was added dropwise, and the solution was kept overnight under reflux. The obtained light-yellow mixture liquid was heating reaction at 100 °C via the rotary evaporator. The liquid was further characterized with Fourier transform infrared (FTIR) and NMR analysis (ESM Figure S1, S2 and S3).

4.5 Modification of CN@ZF-Ms with IL

A simple mixing strategy was used to modify the surface of synthesized CN@ZF-Ms with IL. Typically, the synthesized material and IL were mixed together in a weight ratio of 9:1 and subjected to grinding and sonication for homogenous mixing. Next, the surface of a GP electrode was modified and coated with the synthesized material by simple dip coating (ESM 2.3).

Conflicts of interest

"There are no conflicts to declare".

Acknowledgements

The acknowledgements come at the end of an article after the conclusions and before the notes and references.

Notes and references

1 Chan, E.; Griffiths, S., The implication of water on public health: the case of China. *Perspectives in public health* **2010,** *130* (5), 209-210.

2 (a) Smith, A. H.; Hopenhayn-Rich, C.; Bates, M. N.; Goeden, H. M.; Hertz-Picciotto, I.; Duggan, H. M.; Wood, R.; Kosnett, M. J.; Smith, M. T., Cancer risks from arsenic in drinking water. *Environmental health perspectives* **1992,** *97*, 259-267; (b) Majid, E.; Hrapovic, S.; Liu, Y.; Male, K. B.; Luong, J. H., Electrochemical determination of arsenite using a gold nanoparticle modified glassy carbon electrode and flow analysis. *Analytical chemistry* **2006,** *78* (3), 762-769.

3 (a) Gao, C.; Yu, X.-Y.; Xiong, S.-Q.; Liu, J.-H.; Huang, X.-J., Electrochemical detection of arsenic (III) completely free from noble metal: Fe3O4 microspheres-room temperature ionic liquid composite showing better performance than gold. *Analytical chemistry* **2013,** *85* (5), 2673-2680; (b) Dai, X.; Nekrassova, O.; Hyde, M. E.; Compton, R. G., Anodic stripping voltammetry of arsenic (III) using gold nanoparticle-modified electrodes. *Analytical chemistry* **2004,** *76* (19), 5924-5929.

4 Smedley, P. L.; Kinniburgh, D. G., A review of the source, behaviour and distribution of arsenic in natural waters. *Applied geochemistry* **2002,** *17* (5), 517-568.

5 (a) Munoz, E.; Palmero, S., Analysis and speciation of arsenic by stripping potentiometry: a review. *Talanta* **2005,** *65* (3), 613-620; (b) Jain, C.; Ali, I., Arsenic: occurrence, toxicity and speciation techniques. *Water research* **2000,** *34* (17), 4304-4312.

6 (a) Grabinski, A. A., Determination of arsenic (III), arsenic (V), monomethylarsonate, and dimethylarsinate by ion-exchange chromatography with flameless atomic absorption spectrometric detection. *Analytical chemistry* **1981,** *53* (7), 966-968; (b) Wei, C.; Liu, J., A new hydride generation system applied in determination of arsenic species with ion chromatography–hydride generation-atomic fluorescence spectrometry (IC–HG-AFS). *Talanta* **2007,** *73* (3), 540-545.

7 Dai, X.; Compton, R. G., Detection of As (III) via oxidation to As (V) using platinum nanoparticle modified glassy carbon electrodes: arsenic detection without interference from copper. *Analyst* **2006,** *131* (4), 516-521.

8 Holak, W., Determination of arsenic by cathodic stripping voltammetry with a hanging mercury drop electrode. *Analytical chemistry* **1980,** *52* (13), 2189-2192.

9 (a) Li, D.; Li, J.; Jia, X.; Han, Y.; Wang, E., Electrochemical determination of arsenic (III) on mercaptoethylamine modified Au electrode in neutral media. *Analytica chimica acta* **2012,** *733*, 23-27; (b) Sanllorente‐Méndez, S.; Domínguez‐Renedo, O.; Arcos‐Martínez, M. J., Determination of arsenic (III) using platinum nanoparticle‐modified screen‐printed carbon‐based electrodes. *Electroanalysis: An International Journal Devoted to Fundamental and Practical Aspects of Electroanalysis* **2009,** *21* (3‐5), 635-639; (c) Simm, A. O.; Banks, C. E.; Compton, R. G., The electrochemical detection of arsenic (III) at a silver electrode. *Electroanalysis: An International Journal Devoted to Fundamental and Practical Aspects of Electroanalysis* **2005,** *17* (19), 1727-1733.

10 Cox, J. A.; Kulesza, P. J., Electrocatalytic oxidation and determination of arsenic (III) on a glassy carbon electrode modified with a thin film of mixed-valent ruthenium (III, II) cyanide. *Analytical chemistry* **1984,** *56* (6), 1021-1025.

11 Salimi, A.; Mamkhezri, H.; Hallaj, R.; Soltanian, S., Electrochemical detection of trace amount of arsenic (III) at glassy carbon electrode modified with cobalt oxide nanoparticles. *Sensors and Actuators B: Chemical* **2008,** *129* (1), 246-254.

12 (a) Jang, J.; Hong, S.; Lee, J. S.; Borse, P. H.; Jung, O.-S.; Hong, T.; Jeong, E.; Won, M.; Kim, H., Synthesis of zinc ferrite and its photocatalytic application under visible light. **2009**; (b) Cai, C.; Liu, J.; Zhang, Z.; Zheng, Y.; Zhang, H., Visible light enhanced heterogeneous photo-degradation of Orange II by zinc ferrite (ZnFe2O4) catalyst with the assistance of persulfate. *Separation and purification technology* **2016,** *165*, 42-52; (c) Hufnagel, A. G.; Peters, K.; Müller, A.; Scheu, C.; Fattakhova‐Rohlfing, D.; Bein, T., Zinc Ferrite Photoanode Nanomorphologies with Favorable Kinetics for Water‐Splitting. *Advanced Functional Materials* **2016,** *26* (25), 4435-4443.

13 Goya, G.; Rechenberg, H., Magnetic properties of ZnFe2O4 synthesized by ball milling. *Journal of magnetism and magnetic materials* **1999,** *203* (1-3), 141-142.

14 Waqas, M.; Zulfiqar, A.; Ahmad, H. B.; Akhtar, N.; Hussain, M.; Shafiq, Z.; Abbas, Y.; Mehmood, K.; Ajmal, M.; Yang, M., Fabrication of highly stable silver nanoparticles with shape-dependent electrochemical efficacy. *Electrochimica Acta* **2018,** *271*, 641-651.

15 (a) Su, L.; Feng, J.; Zhou, X.; Ren, C.; Li, H.; Chen, X., Colorimetric detection of urine glucose based ZnFe2O4 magnetic nanoparticles. *Analytical chemistry* **2012,** *84* (13), 5753-5758; (b) Liu, W.; Yang, H.; Ma, C.; Ding, Y.-n.; Ge, S.; Yu, J.; Yan, M., Graphene–palladium nanowires based electrochemical sensor using ZnFe2O4–graphene quantum dots as an effective peroxidase mimic. *Analytica chimica acta* **2014,** *852*, 181-188.

16 Sousa, M. H.; Tourinho, F. A.; Rubim, J. C., Use of Raman micro‐spectroscopy in the characterization of MIIFe2O4 (M= Fe, Zn) electric double layer ferrofluids. *Journal of Raman Spectroscopy* **2000,** *31* (3), 185-191.

17 Singh, J. P.; Srivastava, R.; Agrawal, H.; Kumar, R., Micro‐Raman investigation of nanosized zinc ferrite: effect of crystallite size and fluence of irradiation. *Journal of Raman Spectroscopy* **2011,** *42* (7), 1510-1517.

18 Dennison, J.; Holtz, M.; Swain, G., Raman spectroscopy of carbon materials. *Spectroscopy* **1996,** *11* (8).

19 Tholkappiyan, R.; Vishista, K., Influence of lanthanum on the optomagnetic properties of zinc ferrite prepared by combustion method. *Physica B: Condensed Matter* **2014,** *448*, 177-183.

20 Bardhan, A.; Ghosh, C.; Mitra, M.; Das, G.; Mukherjee, S.; Chattopadhyay, K., Low temperature synthesis of zinc ferrite nanoparticles. *Solid state sciences* **2010,** *12* (5), 839-844.

21 Tsierkezos, N. G., Cyclic voltammetric studies of ferrocene in nonaqueous solvents in the temperature range from 248.15 to 298.15 K. *Journal of Solution Chemistry* **2007,** *36* (3), 289-302.

22 Chinnasamy, C.; Narayanasamy, A.; Ponpandian, N.; Chattopadhyay, K., The influence of Fe3+ ions at tetrahedral sites on the magnetic properties of nanocrystalline ZnFe2O4. *Materials Science and Engineering: A* **2001,** *304*, 983-987.

23 Babar, N.-U.-A.; Joya, K. S.; Tayyab, M. A.; Ashiq, M. N.; Sohail, M., Highly Sensitive and Selective Detection of Arsenic Using Electrogenerated Nanotextured Gold Assemblage. *ACS omega* **2019,** *4* (9), 13645-13657.

24 Sonkoue, B. M.; Tchekwagep, P. M. S.; Nanseu‐Njiki, C. P.; Ngameni, E., Electrochemical Determination of Arsenic Using Silver Nanoparticles. *Electroanalysis* **2018,** *30* (11), 2738-2743.

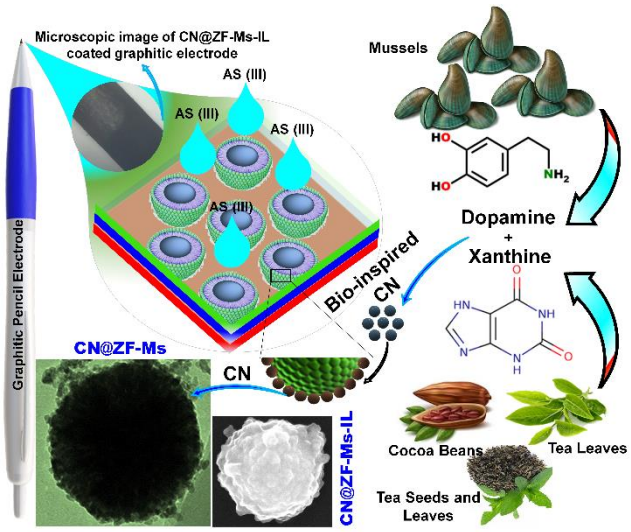

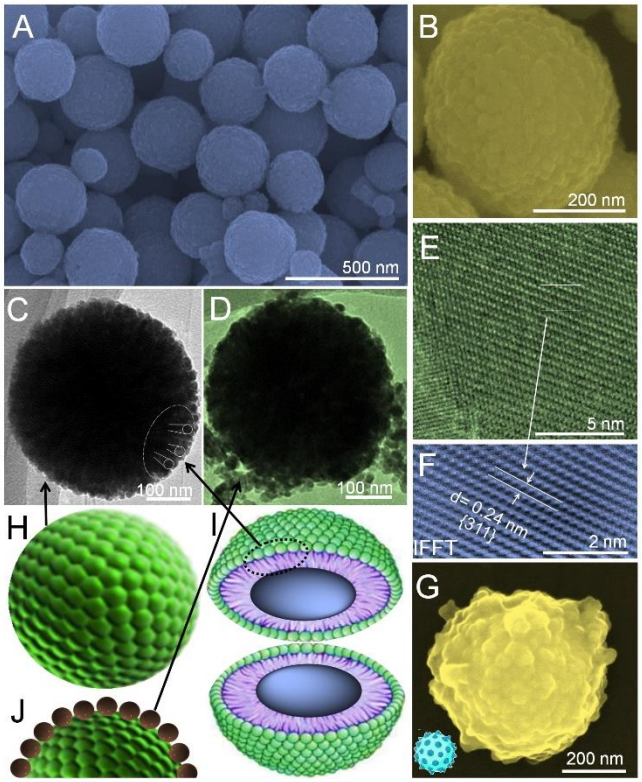

Scheme 1 Schematic diagram representing the construction design of bioinspired CN@ZF-Ms-IL electrode.

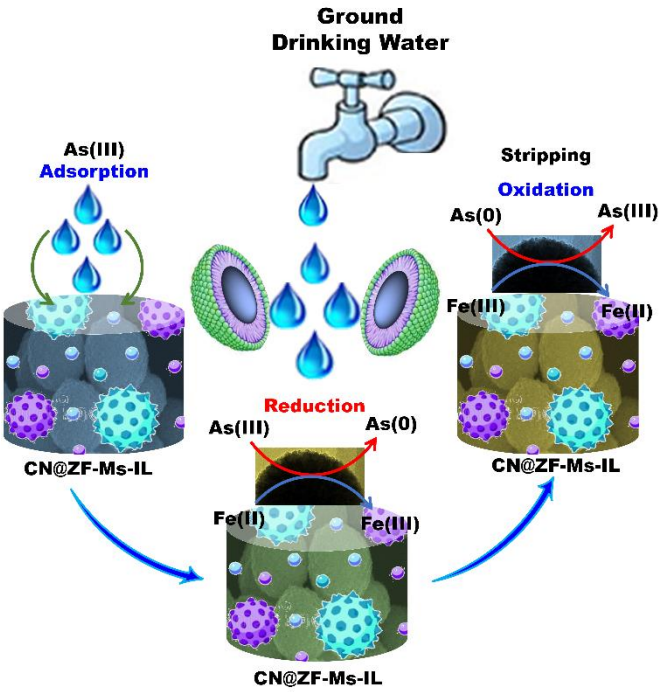

Scheme 2 Schematic diagram showing sensing mechanism of our designed sensor towards As(III).

Figure 1 Low (A) and high magnification (B) FE-SEM image of ZF-Ms respectively, showing uniformity in microspheres. TEM image (C) further confirm the formation of internally inter-connected nanospheres blocks at the surface of microsphere, which are also represented schematically as a whole (H) and cross-sectional view (I). Panel (D) shows the TEM image with clear formation of CN nano-dots at the surface of ZF-Ms with schematic representation in (J). HR-TEM (E) image of ZF-Ms with corresponding IFFT (F). Panel (G) shows SEM image of CN@ZF-Ms modified with IL.

Schemes and Figures

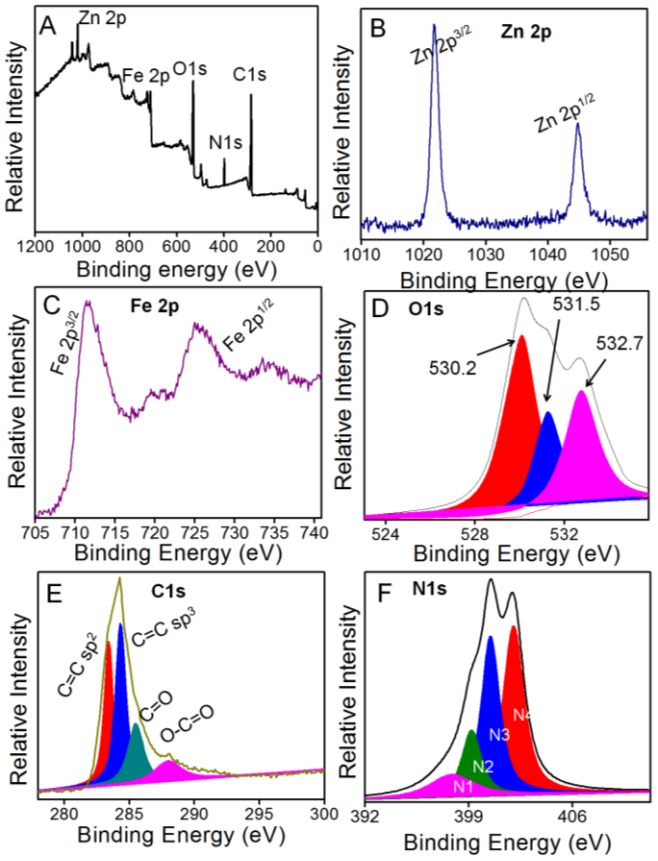

Figure 2 Typical XPS surveys spectra (A) of CN@ZF-Ms indicating peaks corresponding to its all components. Panel (B-F) shows high resolution XPS patterns of Zn, Fe, O, C and N respectively, confirming the successful formation of CN@ZF-Ms.

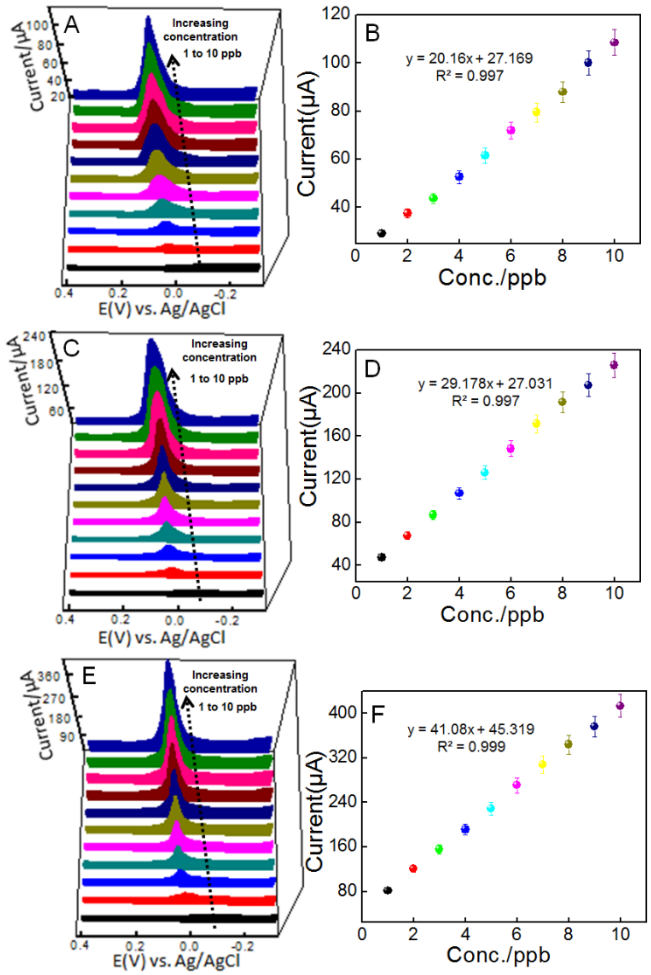

Figure 3 Square wave anodic stripping voltammograms of ZF-Ms (A), CN@ZF-Ms (C) and CN@ZF-Ms-IL (E) towards increasing concentration (1-10 ppb) of As(III) into 0.1 M acetate buffer electrolyte under optimized conditions, whereas Panel (B), (D) and (F) are their respective calibration plots.

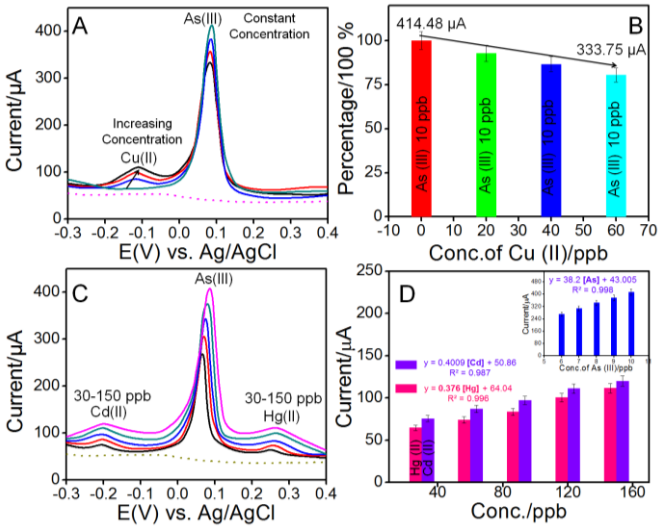

Figure 4 (A) Square wave anodic stripping voltammograms of CN@ZF-Ms-IL (E) towards constant concentration (10 ppb) of As(III) with increasing concentration (20-60 ppb) of Cu(II) in 0.1 M acetate buffer (pH :6). (B) The %age loss of arsenic stripping peak current versus the increasing concentration of Cu(II) derived from (A). Square wave anodic stripping voltammograms (C) of CN@ZF-Ms-IL towards increasing concentrations of Hg(II), Cd(II) and As(III) in 0.1 M acetate buffer (pH :6). (D) Current verses concentration calibration plot derived from Figure 4C.

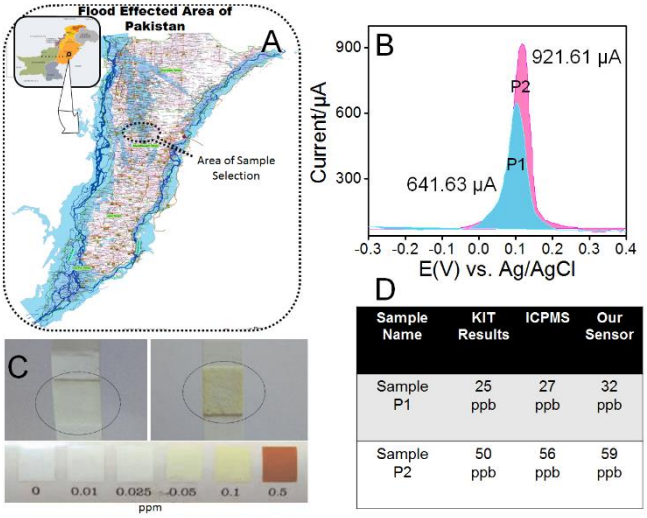

D

Sample Name	KIT Results	ICPMS	Our Sensor
Sample P1	25 ppb	27 ppb	32 ppb
Sample P2	50 ppb	56 ppb	59 ppb

Figure 5 (A) Map of sample collected area, (B) Square wave anodic stripping voltammograms of CN@ZF-Ms-IL towards sample P1 and P2 in 0.1 M acetate buffer (pH :6). (As contamination of sample P1 and P2 was first confirmed through MERCK 117917 Arsenic Test kit). Image c shows the results of sample P2 measured by using MERCK 117917 Arsenic Test kit. (D) shows the comparative results obtained through Kit, ICPMS and our sensor for sample P1 and P2.